

# Effect of Tacticity on the Phase Behavior and Demixing of P $\alpha$ MSAN/dPMMA Blends Investigated by SANS

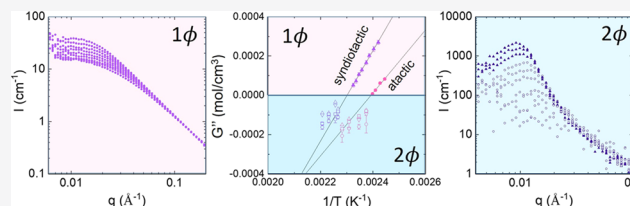
Yutaka Aoki,<sup>†</sup> William Sharratt,<sup>†</sup> Haoyu Wang,<sup>†</sup> Roisin O'Connell,<sup>†</sup> Luca Pellegrino,<sup>†</sup> Sarah Rogers,<sup>‡</sup> Robert M. Dalgliesh,<sup>‡</sup> Julia S. Higgins,<sup>†</sup> and João T. Cabral<sup>\*,†</sup>

<sup>†</sup>Department of Chemical Engineering, Imperial College London, London SW7 2AZ, U.K.

<sup>‡</sup>ISIS, Rutherford Appleton Laboratory, Harwell, Didcot, OX11 0QX, U.K.

## Supporting Information

**ABSTRACT:** We investigate the effect of polymer tacticity on the phase behavior and phase separation of polymer mixtures by small-angle neutron scattering (SANS). Poly( $\alpha$ -methyl styrene-*co*-acrylonitrile) (P $\alpha$ MSAN) and deuterated poly(methyl methacrylate) (dPMMA) with two degrees of syndiotacticity were selected as a model partially miscible blend, as one of the most highly interacting systems known (defined by the temperature dependence of the blend's interaction parameter). One-phase (equilibrium) and time-resolved, spinodal demixing experiments were analyzed by de Gennes' random phase approximation (RPA) and Cahn–Hilliard–Cook (CHC) theory, respectively. The second derivative of the Gibbs free energy of mixing with respect to composition ( $G'' \equiv \partial^2 \Delta G_m / \partial \phi^2$ ) and corresponding  $\chi$  parameter were obtained from both RPA and CHC analysis and found to correlate well across the phase boundary. We find that blends with higher PMMA syndiotacticity exhibit greater miscibility and a steeper  $G''$  temperature dependence by  $\sim 40\%$ . The segment length of dPMMA with higher syndiotacticity was found to be  $a = 7.4$  Å, slightly larger than 6.9 Å reported for lower syndiotacticity dPMMA. Consideration of thermal fluctuations is required for the self-consistent analysis of the nontrivial evolution of the spinodal peak position  $q^*$  over time, corroborated by CHC model calculations. The temperature dependence of the mobility parameter,  $M$ , can be described by a “fast-mode” average of the diffusion coefficients of the blend constituents, except for quenches originating near the glass transition. A minimum demixing length scale of  $\Lambda \approx 40$  nm is obtained, in agreement with the theory for deeper quenches, but deviates at shallower quenches, whose origin we discuss. CHC correctly describes demixing length and time scales, except for quenches into the vicinity of the spinodal boundary. Our data demonstrate the significant effect of relatively minor polymer microstructure variations on polymer blend behavior across both sides of the phase boundary.



One-phase (equilibrium) and time-resolved, spinodal demixing experiments were analyzed by de Gennes' random phase approximation (RPA) and Cahn–Hilliard–Cook (CHC) theory, respectively. The second derivative of the Gibbs free energy of mixing with respect to composition ( $G'' \equiv \partial^2 \Delta G_m / \partial \phi^2$ ) and corresponding  $\chi$  parameter were obtained from both RPA and CHC analysis and found to correlate well across the phase boundary. We find that blends with higher PMMA syndiotacticity exhibit greater miscibility and a steeper  $G''$  temperature dependence by  $\sim 40\%$ . The segment length of dPMMA with higher syndiotacticity was found to be  $a = 7.4$  Å, slightly larger than 6.9 Å reported for lower syndiotacticity dPMMA. Consideration of thermal fluctuations is required for the self-consistent analysis of the nontrivial evolution of the spinodal peak position  $q^*$  over time, corroborated by CHC model calculations. The temperature dependence of the mobility parameter,  $M$ , can be described by a “fast-mode” average of the diffusion coefficients of the blend constituents, except for quenches originating near the glass transition. A minimum demixing length scale of  $\Lambda \approx 40$  nm is obtained, in agreement with the theory for deeper quenches, but deviates at shallower quenches, whose origin we discuss. CHC correctly describes demixing length and time scales, except for quenches into the vicinity of the spinodal boundary. Our data demonstrate the significant effect of relatively minor polymer microstructure variations on polymer blend behavior across both sides of the phase boundary.

## INTRODUCTION

Polymer tacticity impacts thermal, mechanical, rheological, and barrier properties of materials.<sup>1,2</sup> Tacticity affects polymer chain dimensions in solution and melt, effectively modulating local conformation and rigidity of polymer segments,<sup>3–5</sup> as well as the miscibility with other polymers.<sup>6–17</sup> Small-angle neutron scattering (SANS) can be employed to quantify polymer conformation and interactions of partially miscible polymer blends,<sup>18</sup> generally in terms of the random phase approximation (RPA), to yield the segment length of each component  $b$  and an effective interaction parameter  $\chi$ , usually interpreted within the framework of the Flory–Huggins theory.

SANS has been employed to examine the role of tacticity in blends of deuterated polystyrene (dPS), with isotactic and atactic poly(vinyl methyl ether) (iPVME and aPVME).<sup>6</sup> The blend of iPVME/dPS showed steeper temperature dependence of interaction parameter compared to that of aPVME/dPS in the crystalline state of iPVME, while the amorphous state iPVME/dPS was less miscible than aPVME/dS. The more compact conformation of iPVME inferred from the statistical segment length obtained by SANS RPA analysis yields stronger

interaction with dPS per interactive group, which indicates that the configuration affects the phase behavior. However, iPVME undergoes crystallization in the melt state; therefore, the SANS data were treated with care for crystalline melting temperature and interpreted accordingly. To the best of our knowledge, no studies have reported a combined SANS investigation of the demixing and thermodynamic properties of the effect of tacticity in polymer blends, which is the main purpose of this paper.

The effect of PMMA tacticity has been studied from various perspectives, ranging from synthesis methods,<sup>19</sup> glass-transition temperature ( $T_g$ ),<sup>20,21</sup> chain dimensions<sup>3,4</sup> to blend behavior with various polymers.<sup>7–17</sup> These include blends with poly(styrene-*co*-acrylonitrile) (SAN),<sup>16</sup> polycarbonate (PC),<sup>13</sup> poly(vinyl chloride) (PVC),<sup>7,8,10,11,15</sup> and poly(ethylene oxide) (PEO),<sup>9,17</sup> generally reporting that higher syndiotacticity PMMA blends show greater miscibility and attribute the shift of phase boundaries to higher temperatures to the more

Received: October 5, 2019

Revised: December 11, 2019

Published: January 3, 2020

Table 1. Polymer Sample Characteristics<sup>a</sup>

	$\langle M \rangle_w$ [kg/mol]	$\frac{\langle M \rangle_w}{\langle M \rangle_n}$	$m$ [g/mol]	$T_g$ [°C]	$b$ [fm]	$a$ [Å]	$\langle R_g \rangle_w$ [nm]	$h$
PαMSAN	122	2.6	98.66	118 ± 1	21.12	10.1 ± 0.4 <sup>28</sup>	14.5	0.63
dPMMA99k	99.1	1.1	108.1	122 ± 1	98.20	6.9 <sup>29,30</sup>	8.5	10.8
dPMMA110k-s	110	1.1	108.1	127 ± 2	98.20	7.4 ± 0.2	9.6	10.9

<sup>a</sup>Random copolymer PαMSAN comprises 30% AN and 70% α-MSt. The segment length  $a$  for PαMSAN was previously determined<sup>28</sup> and that of dPMMA99k was fixed from literature data.<sup>29,30</sup> Chain dimensions  $R_g$  were computed according to  $\langle R_g \rangle_w = (\langle N \rangle_w a^2 / 6)^{0.5}$  from the tabulated values and polydispersity index  $h \equiv (M_w/M_n - 1)^{-1}$ . Parameter  $b$  is the coherent neutron scattering length, and  $m$  is the mass of each repeat unit.

favorable packing of chains.<sup>13</sup> In terms of the difference in chemical conformation, isotactic PMMA is found in a 10/1 helical conformation with the pitch of 2.11 nm, while syndiotactic PMMA adapts an all-trans conformation; therefore, syndiotactic PMMA can more interact with other polymer species, resulting in better miscibility.<sup>10,11</sup>

Porous polymer materials can be fabricated via demixing induced by a range of methods, which include nonsolvent-induced phase separation, thermally induced phase separation, and reactive blending, with various capabilities and limitations.<sup>22,23</sup> To design bicontinuous structures via thermally induced demixing, a precise understanding of blend thermodynamics is required and, specifically, highly interacting blend systems are needed to achieve nanoscale dimensions through this method.<sup>24,25</sup> In this context, “highly interacting” refers to a deep temperature dependence of blend interaction parameter  $\chi$  such that a large thermodynamic driving force for demixing can be imposed with a modest temperature variation across the phase boundary. Based on our recent overview of spinodal demixing,<sup>25</sup> we select mixtures of poly(methyl methacrylate) (PMMA) with random copolymer poly(α-methyl styrene-co-acrylonitrile) (PαMSAN) as a model system, yielding a lower critical solution temperature (LCST) phase diagram above room temperature and above the glass-transition temperature of both components. The thermodynamics of PαMSAN/dPMMA blends in both the one- and two-phase regions has been investigated by SANS by Higgins et al.,<sup>26</sup> whose demixing yields blends with a faint bluish appearance, associated with the small initial length scale of the spinodal structure (<100 nm), for the conditions investigated. Inspired by this study and the possibility of tuning component interactions with polymer tacticity, we investigate PαMSAN blends with dPMMA of similar molecular mass but varying syndiotacticity, from 63 ± 5% (termed “atactic”) to 78 ± 3% (“syndiotactic”). We systematically investigate near-critical mixtures of these blends, across both sides of the phase boundary, employing isothermal and temperature jump SANS measurements, which we analyze in terms of the RPA and Cahn–Hilliard–Cook (CHC) theories. Our findings demonstrate the significant consequences of modest tacticity changes in the thermodynamics and demixing of a fully amorphous, highly interacting blend.

## EXPERIMENTAL SECTION

**Polymer Mixtures.** Deuterated poly(methyl methacrylate) (dPMMA) with two degrees of syndiotacticity (atactic and syndiotactic) and similar molecular mass (99 and 110 kg/mol) and low polydispersity index (PDI = 1.1), synthesized by living anionic polymerization, was purchased from Polymer Source Inc. Hydrogenous random copolymer poly(α-methyl styrene-co-acrylonitrile) (PαMSAN) with 30% AN and 70% α-MSt (Luran KR2556)<sup>27</sup> was kindly donated by BASF. Glass-transition temperatures  $T_g$  of the pure

components were determined by differential scanning calorimetry (DSC) using a TA Instruments Q2000 with a heating rate of 10 °C/min and computed by the mid-point method (Figure S1). The syndiotacticity (the ratio of racemo–racemo triad) of dPMMA110k-s was determined to be 75% by <sup>1</sup>H NMR and approximately 81% by DSC (Supporting Information Figure S2), and we thus obtain 78 ± 3%; we refer to this sample as syndiotactic, since the value is ≥70%. The dPMMA99k sample is estimated to have a degree of syndiotacticity of 63 ± 5% based on  $T_g$  measurement and its correlation with tacticity,<sup>19,20</sup> detailed in the Supporting Information Figure S2; we refer to this sample as atactic. Key characteristics of the polymer samples used are summarized in Table 1, and the monomer chemical structures are shown in Figure 1.

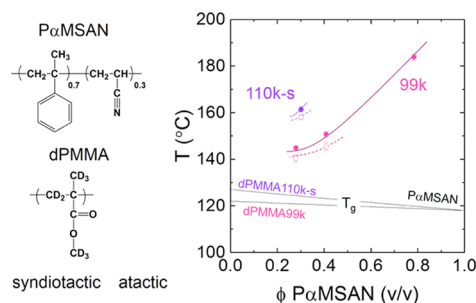


**Figure 1.** Monomer repeat units of PαMSAN and dPMMA and phase diagram of PαMSAN/dPMMA99k (atactic) and dPMMA110k-s (syndiotactic). Filled symbols indicate spinodal temperature from extrapolation of  $G''$  vs  $1/T$ , and open symbols correspond to binodal temperature from Kratky plots, obtained by SANS. Lines serve as a guide to the eye. Black solid lines are  $T_g$  estimates obtained by the Flory–Fox equation and pure component data as given by the Flory–Fox equation.<sup>33</sup>

PαMSAN/dPMMA films were prepared by solution-casting. Selected blend compositions were prepared by mass and then converted into a volumetric ratio of PαMSAN using the pure component densities ( $\rho_{\text{P}\alpha\text{MSAN}} = 1.08 \text{ g/cm}^3$  and  $\rho_{\text{dPMMA}} = 1.28 \text{ g/cm}^3$ ). The polymers were first dissolved in tetrahydrofuran (THF, purity ≥99.7% unstabilized HPLC grade, VWR) at a concentration of 8% w/vol and stirred at room temperature for 48 h. The solution was drop-cast onto glass coverslips (19 mm in diameter, VWR), and the solvent was allowed to evaporate at ambient conditions for 1 week. The resulting films (of approximately 100–150 μm thickness) were then carefully peeled off and placed under vacuum (20 mbar) for 4 weeks, while gradually increasing the temperature up to 110 °C, which is just below the blend  $T_g$ , until no mass changes were observed. Approximately 6–10 films were then stacked together and gently pressed (Specac hydraulic press, 4 ton) at room temperature with an aluminum mold to obtain approximately 1.0 mm thick films for one-phase, isothermal SANS experiments. Before the SANS experiments, the samples were kept in an oven at 125 °C for 36 h and then gradually cooled down to room temperature under vacuum (20 mbar) to prevent the absorption of moisture. Blends of composition PαMSAN/dPMMA99k 28/72, 41/59, 78/22, and PαMSAN/

dPMMA110k-s 30/70 were investigated. The films were then wrapped in a thin aluminum foil (22  $\mu\text{m}$  thick) to be mounted onto a temperature-controlled cell to acquire SANS data in the one-phase region.

The sample preparation procedure was identical for demixing (temperature jump) experiments although, in this case, a single film of 100–150  $\mu\text{m}$  thickness was wrapped in an aluminum foil (minimizing multiple scattering, given the much greater scattering intensity in the two-phase region). In all cases, sample thicknesses were determined using a digital micrometer. For these experiments, we compare P $\alpha$ MSAN/dPMMA99k 28/72 (atactic) and P $\alpha$ MSAN/dPMMA110k-s 30/70 (syndiotactic), which are effectively identical in composition and polymer molecular masses but vary in degree of syndiotacticity. This experimental protocol follows our previous work, examining the effect of composition and  $M_w$  on the phase behavior of this system.<sup>28</sup>

**Small-Angle Neutron Scattering.** SANS experiments were performed at ISIS (U.K.) using diffractometers SANS2D and Larmor and sample to detector distances  $D_{s-d} = 12$  m and 4.1 m, respectively. These configurations yield a momentum transfer  $q = \frac{4\pi}{\lambda} \sin\left(\frac{\theta}{2}\right)$ , where  $\theta$  is the scattering angle, ranging from  $0.0015 < q < 0.5 \text{ \AA}^{-1}$  and  $0.006 < q < 0.6 \text{ \AA}^{-1}$ .

A custom-made brass experimental cell, consisting of two thermally controlled ovens and a mechanical actuator carrying the sample from one (preheating) oven to another (the “experimental oven”), with quartz windows and a 45° exit cone, was employed for both one-phase and demixing experiments.<sup>31</sup> Neutron cloud point experiments were carried out at a heating rate of 2 °C/min from 102 °C (below  $T_g$ ) to above the demixing temperature, to estimate the location of the phase boundaries, as illustrated in Figure 2.

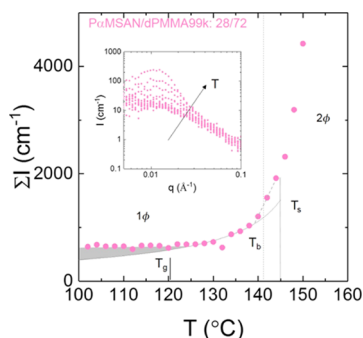


**Figure 2.** Total SANS scattering intensity during a cloud point measurement at heating rate 2 °C/min for P $\alpha$ MSAN/dPMMA99k:28/72. The solid line is computed from RPA in the one-phase region with  $\tilde{\chi}_{12}/\nu_0 = 0.00201 - 0.83/T$ .<sup>28</sup> The binodal  $T_b$ , spinodal  $T_s$ , and glass-transition  $T_g$  temperatures are indicated by vertical lines. The dashed line shows RPA deviations assigned to nucleation and growth in the metastable region. Nonequilibrium behavior near or below  $T_g$  is shown in gray. The inset, which corresponds to cloud point data at every 4 °C from 102 °C, shows the  $I(q)$  cloud point data as a function of temperature.

For one-phase (isothermal) experiments, only the “experimental” oven was utilized. The film was loaded at 125 °C (the final ex situ preheating oven temperature) into the measurement cell, and the temperature was increased, in a stepwise fashion, to the desired temperature. Intervals of 8 °C near  $T_g$  to 2 °C, near the phase boundary, were sampled. Acquisition times ranged from 120 min near  $T_g$ , where sample equilibration is longer and the neutron scattering intensity is lower ( $I(0) \sim 20 \text{ cm}^{-1}$ ) to 3 min near the phase boundary (for which  $I(0) \sim 60 \text{ cm}^{-1}$ ). We found this time to be sufficient to equilibrate concentration fluctuations at  $q \geq 0.01 \text{ \AA}^{-1}$ , and thus sufficient to accurately estimate  $G''$  (or  $\chi$ ), although low- $q$  deviations were observed (corresponding to long-wavelength fluctuations). Data acquisition for a neat P $\alpha$ MSAN 1 mm sample (used to estimate

incoherent contribution) and the empty cell background (arising from aluminum foil and quartz windows) was carried out for 30 min. All data were acquired in time-of-flight “event mode”, which enables the temporal slicing of data after the experiment, during data analysis. This feature is important to ascertain sample equilibration and to adapt time resolution to the magnitude of intensity changes and available data statistics.

Scattering data were reduced and calibrated, and the contribution from the empty cell was subtracted, using Mantid.<sup>32</sup> The self-consistency of sample thickness, neutron transmission, and incoherent background intensity was verified to ensure accurate data calibration. The coherent scattering profile was then obtained by subtraction of the appropriate volume fraction of P $\alpha$ MSAN incoherent contribution.

## RESULTS AND DISCUSSION

**Phase Diagram of P $\alpha$ MSAN/dPMMA Blends.** The phase diagram for both P $\alpha$ MSAN/dPMMA99k and dPMMA110k-s blends, with varying syndiotacticity, is shown in Figure 1, along with the glass-transition temperatures. The spinodal temperatures (solid lines),  $T_s$ , were determined by extrapolation of  $G'' \equiv \partial^2 \Delta G_m / \partial \phi^2$  with inverse temperature, obtained from the forward SANS scattering intensity as  $1/S(0) \equiv G''$  for all compositions, as detailed below. The binodal temperatures (dashed lines),  $T_b$ , were estimated from deviations from RPA analysis in the Kratky representation. Our first observation is that the phase boundaries for P $\alpha$ MSAN/dPMMA110k-s occur at a higher temperature ( $\approx 16$  °C) above those of P $\alpha$ MSAN/dPMMA99k, indicating greater component miscibility for syndiotactic dPMMA (and despite its slightly higher  $M_w$  of 110 kg/mol). The critical point for both blends is located at P $\alpha$ MSAN  $\lesssim 0.3$  (v/v), corroborated by optical microscopy data. For completion, the glass-transition temperature  $T_g$  of the blends is also shown, computed from the Flory–Fox expression  $1/T_{g,\text{blend}} = \phi_{\text{P}\alpha\text{MSAN}}/T_{g,\text{P}\alpha\text{MSAN}} + \phi_{\text{dPMMA}}/T_{g,\text{dPMMA}}$ , based on the pure component values, indicated in Table 1. The proximity between the phase boundary and  $T_g$  is expected to be beneficial in terms of resolving the kinetics of demixing; however, the narrow temperature window ( $\approx 20$ – $30$  °C) between the two transitions also poses challenges to ensure thermal equilibration of concentration fluctuations within the one-phase region.

**SANS Cloud Point Measurements.** Prior to all isothermal experiments, SANS cloud point measurements were carried out at a heating rate of 2 °C/min from 102 to 150 °C, to estimate the location of  $T_b$  and  $T_s$ , as shown in Figure 2 for a P $\alpha$ MSAN/dPMMA99k:28/72 blend. The total scattering intensity ( $\Sigma I$ ) was plotted against temperature, and various regimes could be identified: below  $T_g$ , no intensity changes are observed, as expected; between  $T_g$  and  $T_b$ , the scattering intensity increases gradually, within the one-phase region; a change of slope is observed at both  $T_b$  and  $T_s$ . Based on the (isothermal) data analysis presented below, the temperature dependence of  $G''$  (and  $\chi$ ) and chain conformation was established, allowing the superposition of the RPA theory prediction alongside the cloud point data. There is good agreement between measurement and RPA prediction from  $\approx 126$  °C (above  $T_g$ ) to  $\approx 140$  °C (near binodal for this mixture), within the one-phase region. Under isothermal conditions, the samples did not reach equilibrium even after 36 h of annealing at 125 °C due to the proximity of  $T_{g,\text{blend}} = 120.9$  °C, and this out-of-equilibrium region is shown as a shaded area in Figure 2. Above  $T_b \approx 140.5$  °C, scattering data also gradually deviates from RPA, as expected within the

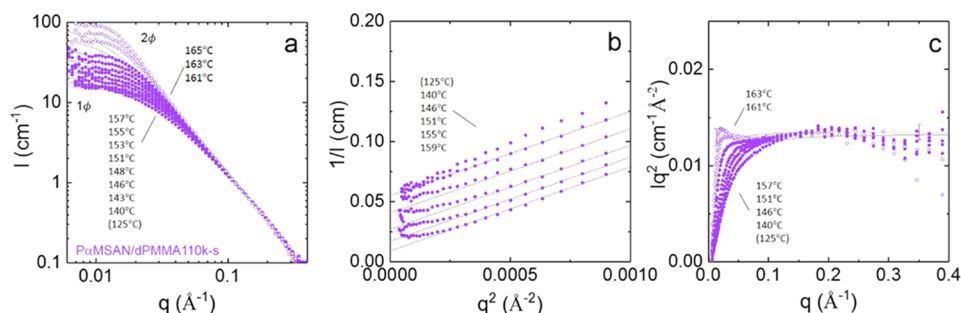


**Figure 3.** (a) Coherent SANS scattering data for P $\alpha$ MSAN/dPMMA110k-s (syndiotactic) obtained by sequential isothermal measurements. Filled symbols correspond to the one-phase region, while open symbols indicate the two-phase region, estimated from the emergence of a peak and departure from RPA scaling. Due to the proximity to  $T_g$ , data at 125 °C (despite annealing for 37 h) are not at equilibrium; RPA deviations are also found at low- $q$  interpreted as due to (expected) slow equilibration of long concentration fluctuations. (b) Ornstein–Zernike plots of the one-phase data shown in (a), which are all described by RPA, with deviations discussed above. (c) Kratky plot of the one-phase (filled symbols) and two-phase (open symbols) data, with lines computed using RPA at the highest and lowest temperatures yielding  $a_{\text{dPMMA110k-s}} = 7.4 \pm 0.2$  Å and fixing  $a_{\text{P}\alpha\text{MSAN}}$  to be 10.1 Å.<sup>28</sup> Open symbols correspond to the SANS data in the two-phase region (which deviate from the RPA by more than a factor of 2), whose lowest temperature is taken as the estimate for the binodal.

metastable region, where demixing takes place by nucleation and growth. A clear peak emerges on the scattering profile between 142 and 146 °C, which agrees with  $T_s$  estimations obtained from SANS isothermal experiments, of 144.8 °C for this blend.

#### RPA Analysis in the One-Phase (Equilibrium) Region.

The coherent scattering intensity  $I(q)$  from a polymer blend in the one-phase region is written by

$$I(q) = N_A \left( \frac{b_1}{v_1} - \frac{b_2}{v_2} \right)^2 S(q) \quad (1)$$

where  $N_A$  is the Avogadro number,  $S(q)$  is the structure factor,  $b_i$  is the coherent scattering length of monomer unit  $i$ , and  $v_i$  is the monomer molar volumes of unit  $i$ . In the following discussion, we refer to component 1 as P $\alpha$ MSAN and 2 as dPMMA, for which  $b_1 = 21.12$  fm,  $v_1 = 91.77$  cm<sup>3</sup>/mol,  $b_2 = 98.20$  fm,  $v_2 = 84.79$  cm<sup>3</sup>/mol, yielding a contrast prefactor  $N_A(b_1/v_1 - b_2/v_2)^2 = 5.19 \times 10^{-3}$  cm<sup>-4</sup> mol. The structure factor  $S(q)$  of the blend is generally expressed by the mean-field, de Gennes' random phase approximation (RPA),<sup>34</sup> as

$$\frac{1}{S(q)} = \frac{1}{S_1(q)} + \frac{1}{S_2(q)} - 2 \frac{\tilde{\chi}_{12}}{v_0} \quad (2)$$

where  $S_i(q)$  [cm<sup>3</sup>/mol] is the structure factor of each component, and  $\tilde{\chi}_{12}$  is an effective specific interaction parameter. Taking component polydispersity into account,  $S_i(q)$  reads<sup>35</sup>

$$S_i(q) = \phi_i v_i \langle N_i \rangle_n \langle g_D(R_g^2 q^2) \rangle_w \quad (3)$$

where  $\phi_i$  is the volume fraction,  $v_0$  is a reference molar volume taken as  $v_0 \equiv \sqrt{v_1 v_2}$ , and  $\langle N_i \rangle_n$  is the number average degree of polymerization of component  $i$ . The weight-average Debye form factor of the polymer chains is  $\langle g_D(x) \rangle_w = \frac{2}{\langle x \rangle^2} \left[ \left( \frac{h}{h+x} \right)^h - 1 + x \right]$ , where  $x \equiv q^2 \langle R_g^2 \rangle_n$  and  $h = (M_w/M_n - 1)^{-1}$ , and the  $n$ -average radius of gyration for a Gaussian coil  $\langle R_g \rangle_n \equiv (\langle N \rangle_n a^2 / 6)^{0.5}$ , where  $a$  is the segment length. In the forward scattering limit,  $q \rightarrow 0$ , eq 2 becomes

$$\frac{1}{S(0)} = \frac{1}{\phi_1 v_1 \langle N_1 \rangle_w} + \frac{1}{\phi_2 v_2 \langle N_2 \rangle_w} - 2 \frac{\tilde{\chi}_{12}}{v_0} \equiv G'' \quad (4)$$

yielding a direct (and model-free) measurement of the second derivative of the free energy with respect to composition,  $G'' \equiv \partial^2 \Delta G_m / \partial \phi^2$ . In the habitual Flory–Huggins lattice framework, the interaction parameter  $\chi$  at the spinodal is

$$\chi_s = \frac{v_0}{2} \left( \frac{1}{\phi_1 v_1 \langle N_1 \rangle_w} + \frac{1}{\phi_2 v_2 \langle N_2 \rangle_w} \right) \quad (5)$$

and therefore, from eq 4, follows that

$$(G'' \equiv) \frac{1}{S(0)} = \frac{2}{v_0} (\chi_s - \tilde{\chi}_{12}) \quad (6)$$

where  $\tilde{\chi}_{12}$  is an effective interaction parameter, measured by SANS, which can be related to the common Flory–Huggins parameter  $\chi_{12}$  by

$$\tilde{\chi}_{12} = -\frac{1}{2} \frac{\partial^2 [\phi(1-\phi)\chi_{12}]}{\partial \phi^2} \quad (7)$$

and thus  $\tilde{\chi}_{12} \equiv \chi_{12}$  for composition-independent interactions. At low angle scattering angles ( $qR_g < 1$ ), the simpler Ornstein–Zernike (OZ) expression provides a good approximation to the data, where

$$S(q) = \frac{S(0)}{1 + \xi^2 q^2} \quad (8)$$

or equivalently

$$\frac{1}{S(q)} = \frac{1}{S(0)} + 2kq^2 \quad (9)$$

where the correlation length is given by  $\xi = \sqrt{2kS(0)}$ , and parameter  $k$  is defined below. The OZ formulation emphasizes that the forward scattering intensity yields a susceptibility  $S(0) \equiv 1/G''$ <sup>36,37</sup> and thus requires no thermodynamic model assumption to obtain  $G''(T)$  and thus characterize blend miscibility.

The coherent scattering data for P $\alpha$ MSAN/dPMMA110k-s:30/70 blends as a function of temperature are shown in Figure 3a, as well as in the Ornstein–Zernike (OZ) and Kratky representations (at selected temperatures) in Figure 3b,c, respectively.

Filled symbols denote data in the one-phase region, which can generally be described by the RPA theory (eqs 1–3),

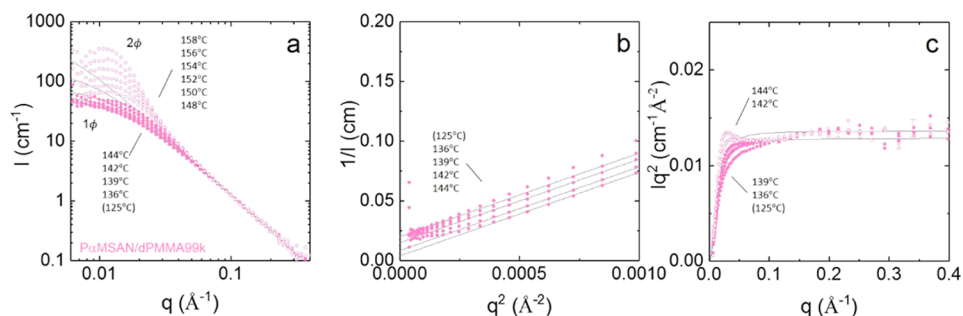


**Figure 4.** (a) Coherent SANS scattering data for  $P\alpha$ MSAN/dPMMA99k (atactic), where filled and open symbols correspond to, respectively, the one- and two-phase regions. Low- $q$  deviations from RPA indicate incomplete equilibration attributed to the proximity to  $T_g$  and finite annealing time during sequential isothermal measurements. (b) Corresponding Ornstein–Zernike plot for data in the one-phase region. (c) Kratky plot for selected data in the one- and two-phase regions, where lines show RPA estimates at the highest and lowest temperatures in the one-phase region corroborating  $a_{P\alpha MSAN} = 10.1 \text{ \AA}$ <sup>28</sup> and  $a_{dPMMA99k} = 6.9 \text{ \AA}$ .<sup>29,30</sup> Open symbols indicate SANS data in the two-phase region ( $q$  power larger than 2), employed to estimate the binodal temperature.

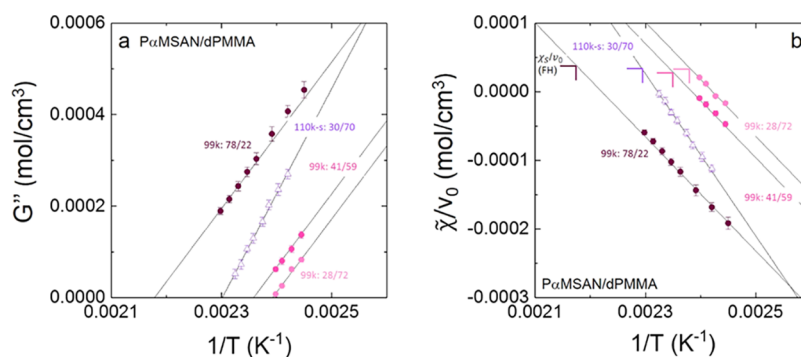


**Figure 5.** (a) Second derivative of free energy of mixing with respect to composition  $G'' \equiv \partial^2 \Delta G_m / \partial \phi^2$  as a function of inverse temperature  $1/T$  for  $P\alpha$ MSAN/dPMMA99k of three distinct compositions 78/22, 41/59, and 28/72 (corresponding to Figure 4 and  $P\alpha$ MSAN/dPMMA110k-s 30/70 (Figure 3)). Lines are fits to  $G'' = \alpha + \beta/T$  with constant slope  $\beta = 1.60$  for  $P\alpha$ MSAN/dPMMA99k and with  $\beta = 2.30$  for  $P\alpha$ MSAN/dPMMA110k-s. (b) Corresponding plot for the effective interaction parameter  $\tilde{\chi}_{12}/v_0$  (computed from eq 4), where the vertical ticks indicate the experimentally measured spinodal temperatures  $T_s$ . Lines are fits to  $\tilde{\chi}_{12}/v_0 = A + B/T$  with constant slope  $B = -0.83$  for  $P\alpha$ MSAN/dPMMA99k and with  $B = -1.55$  for  $P\alpha$ MSAN/dPMMA110k-s.

shown by the solid lines. The initial experimental measurements were conducted at 125 °C following a 37 h annealing (ex situ) in the near-neighborhood of  $T_g$  and found to be out of equilibrium (for instance, by the differing slope in the OZ plot). A stepwise temperature profile (Figure S3) of isothermal measurements was adopted, with equilibration times between steps. At selected temperatures (above 146 °C), the scattering intensity does not fully reach equilibrium at low wavenumbers ( $q \lesssim 0.01 - 0.02 \text{ \AA}^{-1}$ ), corresponding to long-wavelength fluctuations, which is attributed to the proximity to  $T_g$  (and shown by the temporal evolution of the total scattering intensity during an isothermal measurement, shown in Figure S4). We therefore preferentially fit the higher  $q$  region to the RPA model, for which thermal equilibration is achieved within measurement time scales, and take the low- $q$  deviation into account to compute the uncertainty in  $G''$  and  $\tilde{\chi}_{12}$ . This approach is corroborated with the OZ analysis in Figure 3b, showing the parallel linear slopes at all temperatures (bar low- $q$  deviations) and thus intercepts proportional to  $G''$ , as described by eq 9. In the Kratky representation,  $Iq^2$  vs  $q$ , shown in Figure 3c, a peak emerges in the scattering data above 161 °C, also visible in Figure 3a, where open symbols identify data assigned to the two-phase region. The phase boundary is thus estimated to be between 157 and 161 °C, with binodal temperature  $T_b = 159 \pm 2 \text{ }^\circ\text{C}$ . Polymer segment lengths  $a$  were estimated from the Kratky analysis as  $\phi$  and  $v$

are known, since the structure factor of one-phase blends at high wavenumber ( $qR_g \gg 1$ ) can be written as  $S(q)q^2 \approx 12 / \left( \frac{a_1^2}{\phi_1 v_1} + \frac{a_2^2}{\phi_2 v_2} \right)$ . To increase the accuracy of the measurement of  $a$  of dPMMA110k-s, we fix the  $P\alpha$ MSAN segment length to be  $a(P\alpha MSAN) = 10.1 \text{ \AA}$ , measured previously,<sup>28</sup> obtaining  $a(dPMMA110k-s) = 7.4 \pm 0.2 \text{ \AA}$ .

The coherent scattering data for  $P\alpha$ MSAN/dPMMA99k:28/72 (atactic) as a function of temperature are shown in Figure 4a. The coherent scattering data for  $P\alpha$ MSAN/dPMMA99k:41/59 and 78/22 are shown in Figures S5 and S6. As above, the initial 125 °C measurement (following a 36 h ex situ annealing) was found to be out of equilibrium, and data above 139 °C was also found to deviate from RPA at the lowest wavenumbers. A peak in the scattering profile emerges between 144 and 148 °C (beyond which data are shown with open symbols) and therefore  $\sim 10$ – $15 \text{ }^\circ\text{C}$  lower than for the  $P\alpha$ MSAN/dPMMA110k-s blend. The OZ analysis shown in Figure 4b in the one-phase region shows lines of common slope at various temperatures, except at the lowest  $q$  or initial temperature, as expected for RPA, despite incomplete thermal equilibration of long fluctuations. Figure 4c shows the corresponding Kratky plot, from which  $T_b$  is determined to be  $140.5 \pm 1.5 \text{ }^\circ\text{C}$ . Lines are computed from RPA with  $a(P\alpha MSAN) = 10.1 \text{ \AA}$ <sup>28</sup> and  $a(PMMA) = 6.9 \text{ \AA}$ , in agreement

**Table 2.**  $G''$  and  $\tilde{\chi}_{12}/v_0$  of  $P\alpha$ MSAN/dPMMA99k (Atactic) and  $P\alpha$ MSAN/dPMMA110k-s (Syndiotactic) Obtained by SANS in the One-Phase Region, in the Form  $G'' = \alpha + \beta/T$ , and  $\tilde{\chi}_{12}/v_0 = A + B/T$ <sup>a,b</sup>

	$G'' = \alpha + \beta/T$		$\tilde{\chi}_{12}/v_0 = A + B/T$	
	[mol/cm <sup>3</sup> ]		[mol/cm <sup>3</sup> ]	
P $\alpha$ MSAN/dPMMA99k 28/72	−0.003828 + 1.60/T		0.00201 − 0.83/T	
P $\alpha$ MSAN/dPMMA99k 41/59	−0.003773 + 1.60/T		0.00198 − 0.83/T	
P $\alpha$ MSAN/dPMMA99k 78/22	−0.003485 + 1.60/T		0.00184 − 0.83/T	
P $\alpha$ MSAN/dPMMA110k-s 30/70	−0.005293 + 2.30/T		0.00274 − 1.18/T	

<sup>a</sup>Typical confidence limits are  $\pm 0.000004$  and  $0.003$  for  $\alpha$  and  $\beta$ , respectively. <sup>b</sup>The reference volume is taken as  $v_0 \equiv \sqrt{v_1 v_2} = 88.21 \text{ cm}^3/\text{mol}$ . Conversion to reference volume  $v_0 = 100 \text{ \AA}^3$  (often employed to compare systems<sup>38</sup>) is obtained by multiplication of factor  $100/1.66$  (corresponding to  $100 \times N_A/(10^8)^3$  [from mol/cm<sup>3</sup> to / $\text{\AA}^3$ ]).

with the previous literature,<sup>29,30</sup> providing a good description of all one-phase data within measurement uncertainty.

From the analysis so far, we ascertain that the blend syndiotactic dPMMA is more miscible with  $P\alpha$ MSAN, as the phase boundaries shift to a higher temperature (despite the slightly higher  $M_w$ ) and that its segment length also increases to  $7.4 \pm 0.2 \text{ \AA}$ . Next, we examine the effect of tacticity on the component interactions, as measured by  $G''$  or  $\tilde{\chi}_{12}$ .

**Thermodynamics of  $P\alpha$ MSAN/dPMMA Blends in the One-Phase Region.** Figure 5a provides a comparison of  $G''$  as a function of  $1/T$  and all data, at various compositions, which are to follow a linear relation with  $G'' = \alpha + \beta/T$  and slope  $\beta = 1.60 \text{ [mol K/cm}^3]$  and  $\beta = 2.30 \text{ [mol K/cm}^3]$  for dPMMA99k and dPMMA110k-s, respectively. The steep temperature dependence of blend component interactions, and thus large  $\beta$ , indicates the “highly interacting” nature of this partially miscible blend.<sup>25</sup> The steeper slope of  $P\alpha$ MSAN/dPMMA110k-s relative to that of  $P\alpha$ MSAN/dPMMA99k demonstrates that increasing syndiotacticity further increases interaction “strength”, defined by this metric.

Figure 5b plots the effective specific interaction parameter  $\tilde{\chi}_{12}/v_0$  as a function of  $1/T$ , where we define  $v_0 = \sqrt{v_{P\alpha\text{MSAN}} \times v_{\text{dPMMA}}} = 88.21 \text{ cm}^3/\text{mol}$ . Lines are fits to the habitual  $\tilde{\chi}_{12}/v_0 = A + B/T$  with constant slope  $B = -0.83 \text{ [mol K/cm}^3]$  for  $P\alpha$ MSAN/dPMMA99k and with  $B = -1.18 \text{ [mol K/cm}^3]$  for  $P\alpha$ MSAN/dPMMA110k-s. When the reference volume is taken as  $v_0 = 100 \text{ \AA}^3$ ,<sup>38</sup>  $\tilde{\chi}_{12}/v_0 = A + B/T$  in the unit of  $[\text{mol/cm}^3]$  is converted to  $\tilde{\chi}_{12} = A' + B'/T$  in the unit of  $[\text{\AA}^{-3}]$ , where  $A'$  and  $B'$  are computed by multiplying  $A$  and  $B$  by a factor of  $100/1.66$ . All  $G''$  and  $\chi$  parameters, for all compositions investigated, are tabulated in Table 2.

Since  $M_w$  and composition  $\phi$  are nearly identical in both blends, the combinatorial entropy in both cases is similar, viz.  $\Delta S_{\text{combinatorial}} = \frac{1}{\phi_1 v_1 N_1} + \frac{1}{\phi_2 v_2 N_2}$ , or  $\Delta S_{\text{combinatorial}} = 4.9 \times 10^{-5} \text{ mol/cm}^3$  and  $\Delta S_{\text{combinatorial}} = 4.6 \times 10^{-5} \text{ mol/cm}^3$  for  $P\alpha$ MSAN/dPMMA99k and  $P\alpha$ MSAN/dPMMA110k-s, respectively. The contribution to  $\tilde{\chi}_{12}/v_0$  is very small, implying that the greater miscibility of  $P\alpha$ MSAN/dPMMA110k-s must be associated with more favorable (enthalpic or non-combinatorial entropic) specific interactions upon increasing the dPMMA tacticity.

**Cahn–Hilliard–Cook Analysis in the Two-Phase (Spinodal) Region.** When a blend is quenched into the spinodal region, the (initial) evolution of the concentration fluctuation spectrum is generally described by the Cahn–Hilliard (CH)<sup>39,40</sup> and Cahn–Hilliard–Cook (CHC)<sup>41</sup> theories, as detailed by Binder<sup>42</sup> in the context of polymer

blends. Analysis of SANS data requires consideration of thermal fluctuations in the one-phase (equilibrium) region and thus CHC is employed, for which the scattering intensity  $S(q, t)$  is expected to evolve with time according to

$$S(q, t) = S_{T_i}(q) + [S_{T_f}(q) - S_{T_i}(q)] \exp(2R(q)t) \quad (10)$$

where  $S_{T_i}(q)$  is the initial structure factor at the original one-phase temperature  $T_i$ , at a time set as  $t = 0$ . In practical terms,  $T_i$  is the temperature of the preheating oven, and the (equilibrium) scattering intensity is generally well described by the RPA, as given in eq 2. At the final temperature  $T_f$  (corresponding to the experimental oven),  $S_{T_f}(q)$  becomes a “virtual” structure factor, changing sign (becoming negative) below a value  $q^*$ , and cannot thus be directly measured by experiment;  $t$  is the time after the temperature jump, which is assumed to be instantaneous. The virtual structure factor,  $S_{T_f}(q)$ , is computed from eq 9, where  $1/S(0) \equiv G''$  extrapolated to the corresponding  $T_f$  utilizing the relation in Table 2. An illustrate  $S_{T_f}(q)$  is shown in the Supporting Information Figure S8. The growth rate  $R(q)$  of concentration fluctuations is given by

$$R(q) = -Mq^2(G'' + 2kq^2) \quad (11)$$

where  $M$  is a “diffusional mobility” parameter, and  $k$  is the so-called “square gradient term”, capturing the energy penalty of creating an additional interface between demixed phases. In the context of the mean-field approximation of RPA, it can be expressed as

$$k = \frac{1}{6} \left( \frac{\langle R_{g1}^2 \rangle_z}{\phi_1 v_1 \langle N_1 \rangle_w} + \frac{\langle R_{g2}^2 \rangle_z}{\phi_2 v_2 \langle N_2 \rangle_w} \right) = \frac{1}{36} \left( \frac{(h_1 + 2)a_1^2}{(h_1 + 1)\phi_1 v_1} + \frac{(h_2 + 2)a_2^2}{(h_2 + 1)\phi_2 v_2} \right) \quad (12)$$

considering component polydispersity (required for  $P\alpha$ MSAN), where the index  $h$  is given in Table 1 for all samples. The growth rate exhibits a maximum at

$$q^*(\text{CH}) \equiv \sqrt{\frac{-G''}{4k}} \quad (13)$$

yielding a dominant initial length scale of  $\Lambda \approx 2\pi/q^*(t = 0)$  during the early stages of spinodal decomposition, whose duration can be estimated by

$$\tau_c = \frac{1}{2R(q^*(\text{CH}))} = \frac{4k}{MG^{n2}} \quad (14)$$

We have carried out systematic temperature jump experiments into the spinodal region, at near-critical composition, for both blends and employed CHC analysis to extract  $G''$  and  $M$  parameters as a function of temperature. Figure 6 shows the

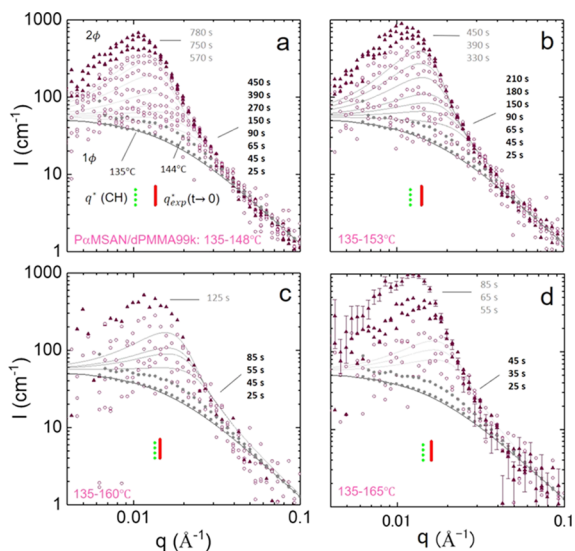


**Figure 6.** Coherent scattering intensity following a time-resolved temperature jump experiment for PaMSAN/dPMMA99k 28/72 from an initial temperature  $T_i = 135$  °C to various final temperatures  $T_f$  of (a) 148 °C, (b) 153 °C, (c) 160 °C, and (d) 165 °C. Open symbols ( $\circ$ ) correspond to early-stage spinodal decomposition data, and filled triangles ( $\blacktriangle$ ) correspond to data outside the early stage. The lines are computed from the Cahn–Hilliard–Cook theory, eq (10), fitting  $G''$  and  $M$ . The gray filled symbols ( $\bullet$ ) correspond to one-phase, isothermal data at  $T_i = 135$  °C and  $T = 144$  °C, which is the highest temperature in the one-phase region measured experimentally. The vertical green dashed line corresponds to  $q^*(\text{CH})$  computed by the maximum position at  $R(q)$  for each jump, and the red solid line to  $q^*_{\text{exp}}(t \rightarrow 0)$ , which is the first experimentally measured peak  $q$  position after the jump. For clarity, representative uncertainties are included in panel (d) for the  $t = 85$  s dataset. As expected in time-of-flight SANS, error bars are larger at both ends of the  $q$  window.

scattering data at various times after jump for PaMSAN/dPMMA99k from common initial temperature  $T_i = 135$  °C to final  $T_f$  of (a) 148 °C, (b) 153 °C, (c) 160 °C, and (d) 165 °C. The experimental realization of temperature jump experiments involves displacing the blend film from the preheating cell (which is set at  $T_i$ ) into the measurement cell ( $T_f$ ), imposing a rapid heating profile (illustrated in Figure S7), which can take  $\sim 30$ – $100$  s, depending on  $\Delta T \equiv T_f - T_i$ . For consistency, we define the initial time  $t = 0$  from the initial jump, although thermal equilibration will occur a few tens of seconds after  $t = 0$ , effectively limiting the shortest time resolution accessible in demixing kinetics. We fit all data with CHC, following eqs 10 and 11, by adjusting  $G''$  and  $M$  and ensuring self-consistency with the early-stage assumptions, including that the data fall within the early-stage  $\tau_c$  estimation. Time points indicated in black (filled triangles) and gray (filled circles) correspond to values inside and outside the early-stage time interval, respectively. In all panels, we include the equilibrium scattering data and RPA profile at  $T_i = 135$  °C (the initial temperature), as well as for  $T = 144$  °C, the highest one-phase temperature measured experimentally for this blend.

The CHC model well describes scattering data for jumps to  $T_f = 148$  °C and 153 °C, but not as well for the deeper

quenches at  $T_f = 160$  °C and 165 °C, which we interpret as due to the short  $\tau_c$  (commensurate with thermal equilibration time following the jump) and data scatter due to short integration times. The solid lines correspond to CHC fits within the early stages of spinodal decomposition. The vertical red lines mark the position in  $q$ , where the first peak in the scattering data is experimentally resolved, denoted by  $q^*_{\text{exp}}(t \rightarrow 0)$ , and the green dashed lines correspond to  $q^*(\text{CH})$  computed from the maximum of  $R(q)$  obtained for each temperature jump, effectively corresponding to eq 13. We find that  $q^*(\text{CH})$  appears systematically at lower values than  $q^*_{\text{exp}}(t \rightarrow 0)$  and that the scattering peak moves (albeit slightly) toward lower  $q$ , even during the early stages of spinodal decomposition. This effect is more significant for shallower quenches and becomes nearly imperceptible within measurement uncertainty for the deeper quenches. Evidently, this contrasts with the CH theory, for which the peak position  $q^*$  is independent of time during the early stages of spinodal decomposition.<sup>39,40</sup> However, both positive and negative  $q^*$  shifts during the initial stages of phase separation have been experimentally observed<sup>43–45</sup> and, in some cases, related to coarsening<sup>43</sup> during the early stages. Below, we find our results to be consistent with the expected role of thermal fluctuations, captured by CHC predictions, as discussed below.

Figure 7 shows the time-resolved temperature jump scattering data for blend PaMSAN/dPMMA110k-s: 30/70

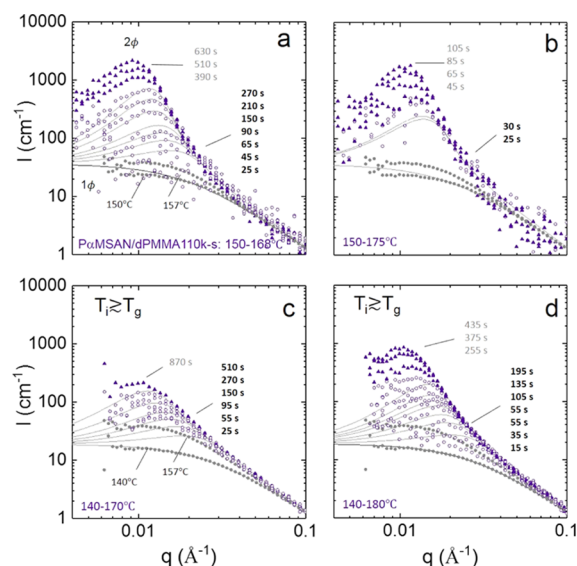


**Figure 7.** Temperature jump experiments for PaMSAN/dPMMA110k-s 30/70 from  $T_i = 150$  °C to  $T_f =$  (a) 168 °C and (b) 175 °C and from  $T_i = 140$  °C to  $T_f =$  (c) 170 °C and (d) 180 °C. As above, open ( $\circ$ ) and closed ( $\blacktriangle$ ) symbols to early- and intermediate-stage spinodal decomposition data, and the lines are fitted to the CHC theory, from eq (10). Gray ( $\bullet$ ) symbols correspond to  $T_i = 150$  °C or 140 °C (with RPA fits), and  $T = 157$  °C, the highest temperature in the one-phase region investigated. Note that  $T_i = 140$  °C in panels (c, d) is just above  $T_g \approx 125$  °C, and deviations from CHC are interpreted as due to the initial out-of-equilibrium state of the sample.

from initial temperature  $T_i = 150$  °C to  $T_f =$  (a) 168 °C and (b) 175 °C and from  $T_i = 140$  °C to  $T_f =$  (c) 170 °C and (d) 180 °C. The one-phase (isothermal) data for  $T = 150$  °C are shown in panels (a,b), as well as the RPA fit. Due to the proximity to  $T_g$ , even after 36 h annealing at 150 °C, the data

show lower scattering intensity at low- $q$  than expected by RPA, which is associated with the incomplete thermal equilibration of long-wavelength concentration fluctuations. The solid lines are CHC fits, showing variable agreement with the experimental data. Lines fit data well for the jumps from 150 °C to 168 °C, shown in Figure 7a, but less well to  $T_f = 175$  °C, which we attribute to the commensurable time scales of thermal equilibration of the sample in the heating cell and  $\tau_c$ . A more complex analysis involving a  $q$ -dependent Onsager mobility term  $\Lambda(q)$  did not significantly improve the agreement with experimental observations. Further, temperature jumps from  $T_i = 140$  °C to both  $T_f = 170$  and 180 °C show significant deviations from CHC analysis, which we attribute to the proximity of  $T_i$  to the glassy state and likely a more complex (time and  $q$ -dependent) mobility parameter  $M$ , discussed below. We next consider our experimental observations of the dominant wavenumber  $q^*$  and corresponding CHC predictions.

#### Dominant $q^*(t)$ : Experiment and CH(C) Theory.

Following the temperature jump into the spinodal region, the location of the scattering intensity maximum  $q_{\text{exp}}^*$  was determined as a function of time  $t$  and shown by the data points in Figure 8 for (a) P $\alpha$ MSAN/dPMMA110k-s for the

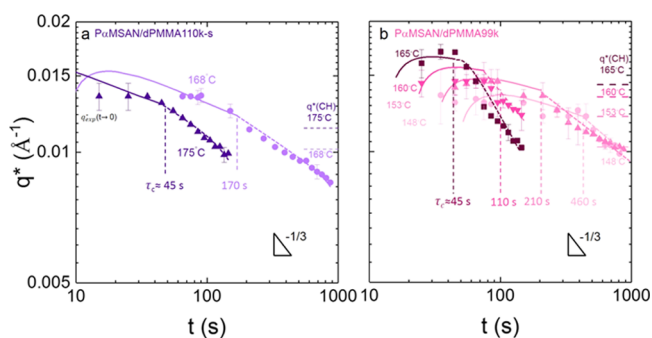


**Figure 8.** Experimentally measured peak position  $q^*$  as a function of time  $t$  after a temperature jump for (a) P $\alpha$ MSAN/dPMMA110k-s from  $T_i = 150$  °C to  $T_f = 168$  °C and 175 °C and (b) for P $\alpha$ MSAN/dPMMA99k from  $T_i = 135$  °C to  $T_f = 148, 153, 160,$  and 165 °C. The solid lines are computed numerically from the CHC theory during the early stage of spinodal decomposition, whose upper time limit is indicated by the vertical lines at  $\tau_c$ . The dashed lines are guides to the eye after  $\tau_c$ , during the intermediate stage. The dominant  $q^*(\text{CH})$  (indicated on the right axis) and  $\tau_c$  at each temperature are determined theoretically by the maximum  $R(q^*)$  using  $G''$  and  $M$  obtained from Figures 6 and 7. A power law corresponding to  $q \propto t^{-1/3}$  is indicated for reference.

two jumps from  $T_i = 150$  °C and (b) P $\alpha$ MSAN/dPMMA99k for all four jumps from  $T_i = 135$  °C. A striking observation is that the experimentally observed  $q^*(t)$  differs from the linearized CH theory alone,<sup>39,40</sup> given by eq 13, with parameters  $G''$  and  $k$  corresponding to that temperature and blend composition. Those are indicated by the horizontal dashed lines at the respective temperatures and are systematically lower than the  $q^*(t)$  observed experimentally during the initial stages of spinodal decomposition. We therefore numerically compute the peak positions of the scattering intensity based on the CHC theory, considering the additional contribution of thermal fluctuations, as given by eq 10, and fixing the parameters obtained from the analysis shown in Figures 6 and 7 (and thus “parameter-free” in this sense). The solid lines in Figure 8 correspond to those estimations and agree well with the experimental data, within measurement uncertainty, during the early stage (i.e., up to the respective  $\tau_c$  for each condition). We note that the theoretical CHC prediction yields a variation of  $q^*$  even during the early stages, and this curvature contrasts with the time-independent  $q^*$  expected for the CH theory. While our data would also be compatible with a time-independent initial  $q^*$ , the experimentally observed  $q_{\text{exp}}^*(t \rightarrow 0)$  would then differ from the corresponding  $q^*(\text{CH})$  calculated theoretically.

Here,  $\tau_c$  is computed from eq 14 using the same  $G''$  and  $M$  as in the data fits reported in Figures 6 and 7. Table 3 tabulates all values for  $q^*$  and  $\tau_c$ . The experimental duration of the early stage of spinodal decomposition  $\tau_{\text{exp}}$  is separately determined by the duration for which  $q_{\text{exp}}^*$  follows the line predicted by the CHC theory and is found to be in good agreement with  $\tau_c$ . Beyond the early stage (as defined by  $\tau_c$ ), we observe  $q^*(t) \propto t^{-1/3}$  for P $\alpha$ MSAN/dPMMA99k 135–165 °C, indicating coarsening by evaporation–condensation or Brownian coalescence, characteristic of this common  $-1/3$  scaling. The exponent  $\alpha$  in  $q^*(t) \propto t^\alpha$  for other temperature jumps is found to be less than  $-1/3$ , suggesting that those data correspond to the crossover from the early to intermediate stages.

Overall, we conclude that CHC provides a fully self-consistent description of all demixing data (which the CH theory alone lacks), with a single set of parameters, and thus that the role of thermal fluctuations must be considered to obtain a comprehensive picture of thermally induced spinodal decomposition. The observed scattering intensity maximum  $q_{\text{exp}}^*(t)$  must therefore be computed from numerical CHC calculations, which are trivial, to yield comprehensive data modeling. We further explore the implications of thermal fluctuations, and the impact of  $T_i$  and  $T_f$  in the next section.

**Table 3.** Tabulated Values  $q^*$ ,  $\tau$ ,  $q(\text{CH})$ , and  $\tau_c$  of All Temperature Jumps for P $\alpha$ MSAN/dPMMA110k-s 30/70 ( $T_s = 161.4$  °C) and P $\alpha$ MSAN/dPMMA99k 28/72 ( $T_s = 144.8$  °C)<sup>a</sup>

dPMMA	$T_i$ (°C)	$T_f$ (°C)	$\Delta T \equiv T_f - T_s$ (°C)	$q_{\text{exp}}^*(t = 0)$ (Å <sup>-1</sup> )	$\tau_{\text{exp}}$ (s)	$q^*(\text{CH})$ (Å <sup>-1</sup> )	$\tau_c$ (s)
110k-s	150	168	6.6	0.0134	170	0.0102	170
	150	175	13.6	0.0135	30	0.0114	45
99k	135	148	3.2	0.0135	450	0.0103	460
	135	153	8.2	0.0141	210	0.0121	210
	135	160	15.2	0.0144	90	0.0134	110
	135	165	20.2	0.0160	60	0.0143	45

<sup>a</sup>The uncertainty in temperature values is  $\approx 1$  °C; the error bars for  $q_{\text{exp}}^*$  are indicated in Figure 8 and range between 10 and 20% for  $\tau$ .

### Impact of Thermal Fluctuations on the Observed $q^*(t)$ . Figure 9a,b shows the calculated evolution of scattering

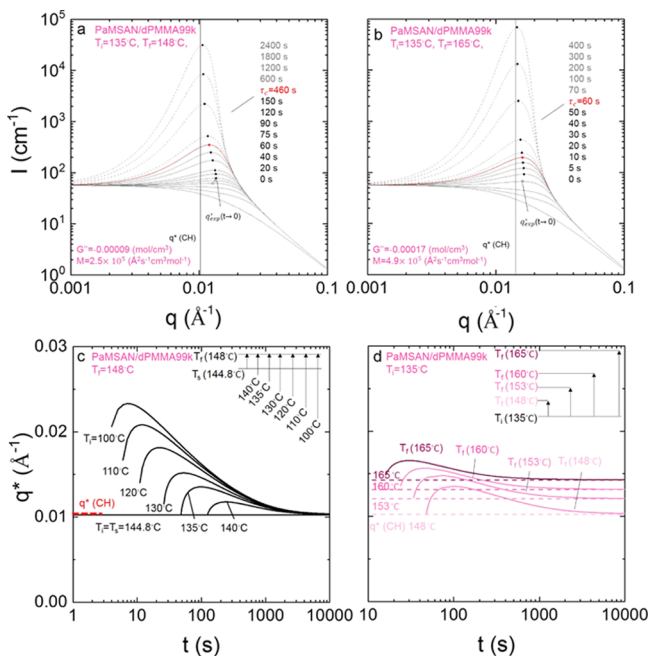


**Figure 9.** Simulated coherent scattering intensity  $I(q, t)$  following the CHC theory and eqs 1 and 10 using the  $G''$  and  $M$  values fitted in (a) Figure 6a and (b) Figure 6d. Filled circles ( $\bullet$ ) indicate the maximum position in each profile, and the red marker corresponds to the maximum at  $\tau_c = 1/2R(q^*)$ . The dashed lines indicate times  $t > \tau_c$  and thus outside the expected validity of CHC. (c, d) Computed  $q^*$  obtained numerically from CHC as a function of time for PaMSAN/dPMMA99k at (c) various initial temperatures from  $T_i = 100^\circ\text{C}$  to  $T_i = T_s$  and (d) various final temperatures from  $T_f = 148^\circ\text{C}$  to  $T_f = 165^\circ\text{C}$ .  $G''$  at each initial temperature is computed from  $G'' = 0.00383 + 1.60/T$  and  $M$  at each jump given in Figure 6. The horizontal dashed lines indicate  $q^*(\text{CH})$  as obtained from  $q^* = \sqrt{-G''/4k}$ , corresponding to the maximum in  $R(q)$  at each temperature.

intensity  $I(q, t)$  based on the CHC theory for a shallower ( $T_i = 135^\circ\text{C}$  to  $T_f = 148^\circ\text{C}$ ) and a deeper ( $T_i = 135^\circ\text{C}$  to  $T_f = 165^\circ\text{C}$ ) quench, from the same initial one-phase temperature. We simulate the evolution of the scattering intensity from eq 10 and based on the experimentally measured parameters for PaMSAN/dPMMA99k, as a function of time (indicated on the graph). These calculations are similar to those reported by Strobl,<sup>46</sup> but here, we have parameterized the results to the blend data and calibrated the curves to absolute units (of  $\text{cm}^{-1}$ ) such that these can be directly compared to experimental scattering profiles. We first note that while the calculations refer to the early stages of spinodal decomposition, the intensity maximum of the scattering profile  $q^*(t)$  is not constant in time, and the peak appears to shift to lower wavenumbers. A more detailed inspection of the evolution of  $q^*(t)$  in time (indicated by markers) shows that it first increases and then decreases (in a trajectory reminiscent of a “boomerang”) in wavenumber over time, before eventually approaching a fixed value at long times. This value is indicated with a solid vertical line and corresponds to the  $q^*(\text{CH})$  as calculated by eq 13 for the parameters employed in the computation of scattering profiles. However, we note that this approach takes place at rather long times, exceeding the duration of the early-stage  $\tau_c$  (indicated by a red marker),

beyond which the linearized treatment is no longer strictly valid as coarsening processes play an increasingly significant role (not included in the computation). Finally, we note that the deeper quench (shown in Figure 9b) shows a smaller departure of  $q^*$  than the shallower quench (Figure 9a), which is not surprising as the relative importance of initial concentration fluctuations expected to become smaller as the driving force for demixing increases. These observations are entirely consistent, quantitatively, with our experimental findings.

Figure 9c,d illustrates the dependence of  $q^*(t)$  during the early stage on  $T_i$  and  $T_f$  with panel (c) considering a fixed  $T_f$  and varying  $T_i$  and panel (d) examining a fixed  $T_i$  and varying  $T_f$  (as generally adopted in experiments). The horizontal dashed lines correspond to  $q^*(\text{CH})$ , and all profiles converge to its corresponding value, at sufficiently long times. In panel (c), we observe that the lower  $T_i$ , the larger the amplitude of the  $q^*$  digression, before approaching  $q^*(\text{CH})$ , compatible with the expectation that the impact of thermal fluctuations diminishes for shorter temperature jumps (and the offset vanishes for  $T_i$  approaches the spinodal temperature  $T_s$ ). Panel (d), however, demonstrates that this effect decreases with increasing  $T_f$  (and thus quench depth) and that deeper quenches approach  $q^*$  faster, as the driving force for demixing is greater, and are less impacted by the initial thermal fluctuations, at constant  $T_i$ . These considerations agree well with the experimental observations reported in the previous section, namely, in Figures 6 and 7, impacting the observed offset between  $q^*$  and  $q^*(\text{CH})$ . Experimentally, we find that this effect can be considerable for the temperature jumps investigated here,  $\Delta T \approx 3 - 20^\circ\text{C}$ , and generally exceeds the wavenumber  $q$  resolution of experimental measurements. Significantly, the measured  $q^*$  does not actually reach  $q^*(\text{CH})$  during the early stage, which is estimated by  $\tau_c$ . We emphasize that while this behavior could be suggestive of coarsening during the early stages of spinodal decomposition as proposed by Rapp and Balsara,<sup>43</sup> the CHC framework can rationalize all data in terms of the well-known effect of thermal fluctuations originating from the one-phase region.

#### Correlation of $G''$ Data across the Phase Boundary.

The second derivative of Gibbs free energy of mixing  $G''$  as a function of inverse temperature  $1/T$ , computed by several analysis methods, in both one- and two-phase regions, is shown in Figure 10. As before, we find that dPMMA110k-s blends show a steeper slope than dPMMA99k blends and that, in both cases, the data obtained from RPA and CHC analysis agree rather well across the spinodal boundary. Such correlations were previously investigated by Han et al.,<sup>47</sup> Higgins et al.,<sup>26</sup> and Schwahn et al.,<sup>48</sup> broadly finding a reasonable agreement between  $G''$  (or equivalent susceptibility) or  $\chi$  parameter computed as described above. While the one-phase  $G''$  ( $>0$ ) data can be obtained to high precision from the RPA analysis and follows the expected linear dependence with  $1/T$ , the two-phase  $G''$  ( $<0$ ) data obtained by CHC analysis is considerably more scattered. For completeness, we compute  $G''$  following four distinct methods, indicated in Figure 10, specifically: from eq 13 and the experimentally observed  $q^*(t \rightarrow 0)$ ; from fitting the highest (+) and lowest (-) values of  $G''$  able to describe the temporal evolution of the scattering profiles with the CHC model, given by eq 10; and from fitting eq 11 to the experimentally measured  $R(q)$  (shown in Figure S10). We find that no method yields a particularly narrow measurement uncertainty, or clearer correlation with one-phase data, and

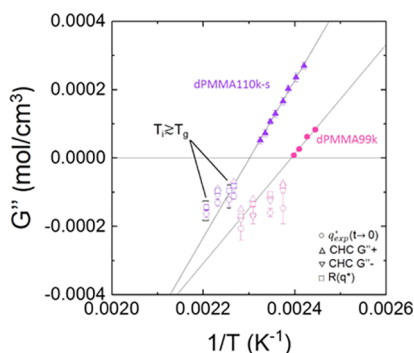


**Figure 10.** Temperature dependence of  $G''$  for  $P\alpha$ MSAN/dPMMA110k-s and  $P\alpha$ MSAN/dPMMA99k on both sides of the phase boundaries. Filled symbols correspond to data obtained from RPA analysis in the one-phase region, yielding the solid lines  $G'' = -0.00383 + 1.60/T$  for  $P\alpha$ MSAN/dPMMA99k and  $G'' = -0.00529 + 2.30/T$  for  $P\alpha$ MSAN/dPMMA110k-s. In the two-phase region,  $\circ$  is computed from  $G'' = -4kq_{\text{exp}}^{*2}(t=0)$ , where  $q_{\text{exp}}^*(t=0)$  is determined experimentally from Figure 8,  $\triangle$  and  $\nabla$  indicate  $G''+$  and  $G''-$  estimated from fitting the CHC theory (eqs 11 and 10) to  $I(q, t)$  data adjusting  $G''$  and  $M$ , and  $\square$  markers are obtained from fitting  $G''$  and  $M$  to experimentally measured  $R(q)$ .

that the slopes of  $G''$  data with  $1/T$  in the two-phase region appear generally lower than those observed in the one-phase region.

We find that the measured  $G''$  for dPMMA99k blends in the two-phase region deviates from the RPA extrapolated line (from the one-phase region) for  $\Delta T \equiv T_f - T_s \lesssim 15.2$  °C. The CHC results from the shallower quenches might be impacted by the commensurable time scales of thermal equilibration in the cell and demixing, effectively resulting in a “slow” (or at least slower, as shown in Figure S11) quench, compared to those at larger  $\Delta T$ .

Deviations from mean-field behavior could also potentially cause such offsets in the data and are expected near the critical point, on either side of the phase boundary, where concentration fluctuations dominate. The Ginzburg criterion estimates the temperature range associated with such deviations and, while several definitions are possible,<sup>48–51</sup> we estimate  $\Delta T < 3$  °C to be smaller than those observed experimentally. Overall, however, apart from near  $T_s$ , the correlation between  $G''$  data across the phase boundaries appears to be rather consistent.

**Mobility Parameter  $M$ .** We next consider the experimental results for the mobility parameter  $M$  and compare these with theoretical models. We tentatively write  $M$  as a combination of the individual diffusion coefficients  $D$  of each component,<sup>25,48</sup> expressed in terms of the fast mode as

$$M = \phi_1 \phi_2 (\phi_1 v_1 D_1 + \phi_2 v_2 D_2) \quad (15)$$

where  $D$  for each polymer component is given by reptation in this  $q$  range and thus

$$D = \frac{k_B T d_T^2}{3N^2 \zeta a^2} \quad (16)$$

where  $k_B$  is the Boltzmann constant,  $d_T$  is the tube diameter of  $\sim 6$  nm,<sup>25</sup> and  $\zeta$  is the monomer friction coefficient and unit of  $D$  is  $[\text{cm}^2/\text{s}]$ . We fix the PMMA monomer friction coefficient to  $\zeta_{\text{dPMMA}} = 0.04/T - 8.12 \times 10^{-5}$  [dyn s/cm]<sup>52,53</sup> and fit the monomer friction for  $P\alpha$ MSAN from the experimentally

observed  $M$  yielding  $\zeta_{P\alpha\text{MSAN}} = \frac{0.0007}{T} - 1.54 \times 10^{-6}$ , which seems pertinent for this copolymer based on previous data.<sup>52</sup> With these monomer friction coefficients, all data for both dPMMA110k-s and dPMMA99k blends can be rather well described by eq 15, as shown in Figure 11.

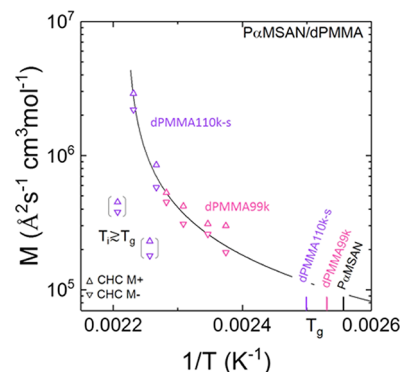


**Figure 11.** Experimentally measured mobility  $M$  as a function of inverse temperature  $1/T$ .  $\triangle$  and  $\nabla$  indicate  $M$  estimated from CHC, and the solid line corresponds to eqs 15 and 16, fixing monomer friction coefficient  $\zeta$  for dPMMA99k and 110k-s as  $\zeta_{\text{dPMMA}} = \frac{0.04}{T} - 8.12 \times 10^{-5}$  [dyn s/cm]<sup>52,53</sup> and adjusting  $\zeta$  for  $P\alpha$ MSAN to be  $\zeta_{P\alpha\text{MSAN}} = \frac{0.0007}{T} - 1.54 \times 10^{-6}$  [dyn s/cm]. The two data points, which deviate from the curve, correspond to T-jumps from  $T_i = 140$  °C near  $T_g$ , interpreted as jumps from an out-of-equilibrium state. The  $T_g$  of pure components is indicated by the vertical lines.

**Initial Spinodal Length Scale Prediction  $\Lambda \equiv 2\pi/q^*(\sim 0)$ .** We next consider the ability of CH(C) theory to predict the initial length scale of the spinodal structure, based on eq 13 and  $G''$ , against our experimental observations. Four distinct estimates are made, indicated in the top right of the panel, based on four schemes to compute  $\Lambda$  and  $G''(T)$  pairs. Specifically,  $G''$  can be either computed from extrapolation from the one-phase data fitted to RPA, named  $G''(1\phi)$ , or from CHC fitting in the two-phase region; separately, the dominant length scale  $\Lambda$  can be calculated from the model  $q^*(\text{CH})$ , of eq 13, or from the initial location of the intensity maximum,  $q_{\text{exp}}^*(t \rightarrow 0)$ . The solid lines show the theoretical predictions for both systems (with only slightly different  $k$ )

computed from  $\Lambda = 2\pi/\sqrt{\frac{-G''}{4k}}$ , and the data points are labeled according to the legend in Figure 12, obtained from independent criteria. Overall, we find that the length scale prediction for dPMMA99k blends is in good agreement with the data for the two deeper quenches, but the shallower quenches yield smaller  $\Lambda$  from the experiment than the CH theory predictions. Data for dPMMA110k-s blends generally show broad agreement with the CH theory. Length scale predictions  $\Lambda$  based on  $G''(\text{CHC})$  generally show better agreement with the experiment, likely due to the fact that this value is more robust since it is based on the entire dataset and not the peak position alone. Overall, we find that CHC is effective at predicting initial demixing length scales following spinodal decomposition, except for shallow quenches for which both measurement and the validity of theory remain somewhat unclear. This highly interacting blend enables phase sizes as small as  $<40$  nm to be accessed with rather modest ( $\sim 10$  °C)

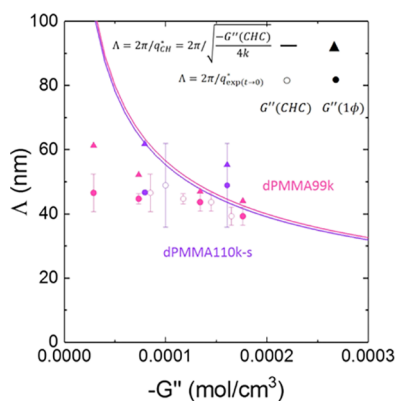


**Figure 12.** Initial spinodal length scale  $\Lambda \equiv 2\pi/q^*$  as a function of  $-G''$  obtained for  $P\alpha$ MSAN/dPMMA110k-s and  $P\alpha$ MSAN/dPMMA99k. Four distinct estimates are made, indicated in the top right of the panel (detailed in the text). In short,  $G''(1\phi)$  is computed from extrapolation from the one-phase data fitted to RPA, while  $G''(\text{CHC})$  is obtained from fitting two-phase kinetic data; wavenumber  $q^*$  is either determined directly from the data, as  $q_{\text{exp}}^*(t \rightarrow 0)$ , or computed from  $G''(\text{CHC})$ . Lines are  $\Lambda = 2\pi/\sqrt{\frac{-G''}{4k}}$  with the two corresponding  $k$  values for the atactic and syndiotactic blends.

temperature quenches, and the difference in tacticity of both dPMMA specimens does not change this behavior significantly.

## CONCLUSIONS

We present a detailed SANS study of the thermodynamics and phase separation of  $P\alpha$ MSAN/dPMMA, on both sides of the phase boundary. We comparatively examine blends with two dPMMA samples of similar  $M_w$  and differing in degree of syndiotacticity, termed atactic and syndiotactic according to the customary classification. The impact of the difference of syndiotacticity of dPMMA110k-s of  $78 \pm 3\%$  (syndiotactic) and dPMMA99k of  $63 \pm 5\%$  (atactic) on the blend thermodynamics is experimentally examined in detail. This partially miscible blend is one of the most highly interactive systems known, in terms of the steepness of the dependence of  $G''$  (or corresponding  $\chi$ ) with  $1/T$ , which implies that a small temperature variation can cause a significant response in  $G''$ . We are motivated by the potential of achieving nanoscale phase dimensions via thermally induced spinodal decomposition, which requires both rapid temperature quenches and a large variation of component interactions  $G''$  to avoid slow or “noninstantaneous”<sup>54</sup> quenches unable to attain small phase sizes. From previous reports,<sup>25,26</sup> this blend should yield spinodal structures of a few tens of nanometers to be formed with  $\sim 10$  °C thermal quenches, which can be readily implemented in practice. In a previous publication,<sup>28</sup> we investigated the role of  $M_w$  and blend composition  $\phi$  on phase behavior and demonstrated the formation of spinodal structures of initial phase size of  $\sim 35$  nm. In this paper, we examine whether a modest change in polymer (dPMMA) tacticity can significantly alter blend thermodynamics. Based on SANS measurements across a range of temperatures in the one-phase, equilibrium region of the phase diagram, and employing RPA analysis, we demonstrate that blends with syndiotactic dPMMA exhibit steeper  $G''(1/T)$  dependence by approximately 40% and also a slightly larger polymer segment length (by  $\approx 7\%$ ). Specifically, we obtain  $G'' = -0.00383 + 1.60/T$  [mol/cm<sup>3</sup>] for atactic blend  $P\alpha$ MSAN/dPMMA99k 28/72 and  $G'' = -0.00529 + 2.30/T$  [mol/cm<sup>3</sup>] for

syndiotactic blends (corresponding to  $\tilde{\chi}_{12}/v_0 = 0.00201 - 0.83/T$  and  $\tilde{\chi}_{12}/v_0 = 0.00274 - 1.18/T$  [mol/cm<sup>3</sup>], respectively). We find that the increase in syndiotacticity causes an upward shift in the LCST phase boundary by  $\approx 20$  °C for  $P\alpha$ MSAN/dPMMA110k-s, with respect to  $P\alpha$ MSAN/dPMMA99k, and therefore an increase in the miscibility window. Given the dependence of the theoretically predicted spinodal (initial) length scale as  $\Lambda \equiv 2\pi/q^* = 2\pi/\sqrt{\frac{-G''}{4k}}$ , we could thus expect smaller phase sizes with the dPMMA blend of higher syndiotacticity.

A number of temperature jump experiments from the one-phase region into the spinodal, unstable, region were carried out by SANS and analyzed by the Cahn–Hilliard–Cook (CHC) theory for both dPMMA110k-s and dPMMA99k blends. The influence of thermally driven concentration fluctuations is significant and captured by the CHC theory, including the initial  $q^*$  time dependence during the early stages of spinodal decomposition. As concentration fluctuations are significant and well resolved by SANS,  $q^*$  is not expected to be constant in time, even at early times. CHC analysis provides an independent measurement of  $G''$ , which is negative within the spinodal region, and found to correlate reasonably well with one-phase  $G''$  measurements across the phase boundary. Deviations from the theory are observed when the initial jump temperature  $T_i$  is near  $T_g$ , and possible explanations are discussed.

We find that the mobility term  $M$ , setting the kinetics of demixing alongside the driving force  $G''$ , can be expressed in terms of the diffusion coefficient  $D$  of each polymer component with a fast-mode mixing rule. We obtain a monomer friction coefficient  $\zeta_{P\alpha\text{MSAN}} = \frac{0.0007}{T} - 1.54 \times 10^{-6}$  [dyn s/cm], which describes data from both blends across the temperature range (except for quenches originating from near  $T_g$ ).

The initial spinodal length scale  $\Lambda$  could be well predicted, within measurement uncertainty from the CHC theory and CH theory for both  $P\alpha$ MSAN/dPMMA110k-s and  $P\alpha$ MSAN/dPMMA99k blends. An agreement with the theory becomes less good for shallow quenches within the spinodal, i.e., for  $T_i \geq T_s$ ; this could be possibly due to (expected) deviation from mean-field behavior, but equally from experimental technicalities related to the commensurability of time scales of the temperature change and demixing process, departing from an “instantaneous” quench. The minimum spinodal length scale attained in this study is  $\approx 40$  nm, among the smallest observed by thermally induced demixing.<sup>25</sup> In this particular case, the variation of syndiotacticity does not impact the length scale perceptively: despite the steeper  $G''$  temperature dependence, the upward shift in phase diagram with increasing dPMMA tacticity results in a commensurate  $-G''$  for a similar  $\Delta T$ . Figure 13 shows the dependence of  $\Lambda$  for dPMMA99k and dPMMA110k-s blends with quench depth  $\Delta T \equiv T - T_s$ , computed from the respective  $G'' = \alpha + \beta/T$  relations obtained experimentally. At the quench depths  $\Delta T$  of interest, the difference in the resulting initial spinodal length scale is a modest  $\approx 4$  nm, within experimental uncertainty. The same figure includes simulated results obtained by modifying the  $\alpha$  and  $\beta$  parameters for the  $P\alpha$ MSAN/dPMMA99k blend, indicated by the dashed lines. Decreasing  $\alpha$  decreases both  $\Lambda$  and  $T_s$ , while increasing  $\beta$  increases both  $\Lambda$  and  $T_s$ ; evidently, the  $G''$  parameters for  $P\alpha$ MSAN/dPMMA110k-s

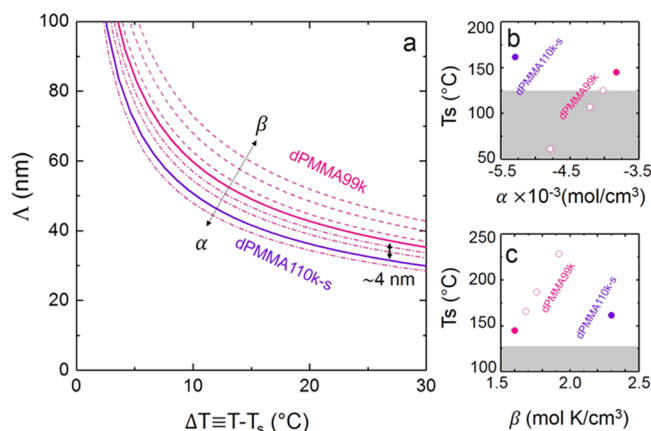


**Figure 13.** (a) Simulated length scale,  $\Lambda$ , as a function of  $\Delta T \equiv T - T_g$  for P $\alpha$ MSAN/dPMMA99k and P $\alpha$ MSAN/dPMMA110k-s blends with varying  $\alpha$  or  $\beta$  in  $G'' = \alpha + \beta/T$ . The red and purple solid lines are computed from  $G'' = -0.003828 + 1.60/T$  and  $G'' = -0.005293 + 2.30/T$  corresponding to P $\alpha$ MSAN/dPMMA99k and P $\alpha$ MSAN/dPMMA110k-s, respectively. The dot-dashed lines correspond to  $G'' = -0.003828 + 1.60/T$  (P $\alpha$ MSAN/dPMMA99k blends) with varying  $\alpha$ . The dashed lines correspond to  $G'' = -0.003828 + 1.60/T$  (P $\alpha$ MSAN/dPMMA99k blends) with varying  $\beta$ . (b, c) Spinodal temperature as a function of  $\alpha$  and  $\beta$ . Filled symbols correspond to our obtained results, and open symbols correspond to  $T_s$  with varying  $\alpha$  and  $\beta$ . The shaded area indicates that blends are in a glassy state.

lead to an increase in both  $\alpha$  and  $\beta$ , and these effects largely “cancel out”, resulting in the relatively small  $\Lambda$  difference. Overall, it is clear that varying polymer tacticity offers a powerful means to modulating polymer blend component interactions. Evidently, this effect cannot be captured by the Flory–Huggins theory and merits a detailed thermodynamic investigation of the noncombinatorial entropic and enthalpic contributions to the free energy of mixing, which we suggest may arise from packing differences caused by the effect of tacticity on the chain conformation. Further work in this area is needed for the predictive design of spinodal structures.

## ■ ASSOCIATED CONTENT

### ● Supporting Information

The Supporting Information is available free of charge at <https://pubs.acs.org/doi/10.1021/acs.macromol.9b02115>.

DSC for P $\alpha$ MSAN, dPMMA110k-s, and dPMMA99k, tacticity dependence of  $T_g$  for PMMA, temperature profiles of SANS isothermal experiments, comparison of SANS intensity and RPA expectation for dPMMA99k one-phase experiments, coherent scattering profiles and OZ plots for dPMMA99k, temperature profile of the measurement cell for the T-jump experiment, quality of T-jump experiments, virtual structure factor, Ginzburg criterion, mobility term for P $\alpha$ MSAN/dPMMA99k and P $\alpha$ MSAN/dPMMA110k-s blends, growth rate for each T-jump, quench depth dependence of  $G''/k$  and length scale, Onsager mobility term for P $\alpha$ MSAN/dPMMA99k and length scale prediction as a function of quench depth (PDF)

## ■ AUTHOR INFORMATION

### Corresponding Author

\*E-mail: [j.cabral@imperial.ac.uk](mailto:j.cabral@imperial.ac.uk). Phone: +44 207 594 5571

## ORCID

William Sharratt: 0000-0003-2148-8423

Haoyu Wang: 0000-0002-6563-8633

João T. Cabral: 0000-0002-2590-225X

## Notes

The authors declare no competing financial interest.

## ■ ACKNOWLEDGMENTS

The authors thank the ISIS neutron source (U.K.) for beamtime and the Engineering and Physical Sciences Research Council (EPSRC, U.K.) for financial support. The authors are grateful to Zhen-Gang Wang (California Institute of Technology) and Jack F. Douglas (National Institute of Standards and Technology) for discussions regarding various forms of the Ginzburg criterion and Daniel Read (University of Leeds) for discussions on polymer diffusion and monomer friction coefficients.

## ■ REFERENCES

- (1) Brandrup, J.; Immergut, E.; Grulke, E. A. *Polymer Handbook*, 4th ed.; Wiley, 1999.
- (2) Lin, C.; Yi, S.; Regen, S. L. Consequences of Tacticity on the Growth and Permeability of Hyperthin Polyelectrolyte Multilayers. *Langmuir* **2016**, *32*, 375–379.
- (3) Yamakawa, H.; Fujii, M. Statistical mechanics of helical wormlike chains. I. Differential equations and moments. *J. Chem. Phys.* **1976**, *64*, 5222–5228.
- (4) Vacatello, M.; Flory, P. J. Conformational statistics of poly(methyl methacrylate). *Macromolecules* **1986**, *19*, 405–415.
- (5) Jones, T. D.; Chaffin, K. A.; Bates, F. S.; Annis, B. K.; Hagaman, E. W.; Kim, M.-H.; Wignall, G. D.; Fan, W.; Waymouth, R. Effect of Tacticity on Coil Dimensions and Thermodynamic Properties of Polypropylene. *Macromolecules* **2002**, *35*, 5061–5068.
- (6) Beaucage, G.; Stein, R. S. Tacticity effects on polymer blend miscibility. 3. Neutron scattering analysis. *Macromolecules* **1993**, *26*, 1617–1626.
- (7) Schurer, J.; de Boer, A.; Challa, G. Influence of tacticity of poly(methyl methacrylate) on the compatibility with poly(vinyl chloride). *Polymer* **1975**, *16*, 201–204.
- (8) Vorenkamp, E.; ten Brinke, G.; Meijer, J.; Jager, H.; Challa, G. Influence of the tacticity of poly(methyl methacrylate) on the miscibility with poly(vinyl chloride). *Polymer* **1985**, *26*, 1725–1732.
- (9) Silvestre, C.; Cimmino, S.; Martuscelli, E.; Karasz, F.; MacKnight, W. Poly(ethylene oxide)/poly(methyl methacrylate) blends: Influence of tacticity of poly(methyl methacrylate) on blend structure and miscibility. *Polymer* **1987**, *28*, 1190–1199.
- (10) Lemieux, E.; Prud'homme, R. E.; Forte, R.; Jerome, R.; Teysse, P. Influence of the tacticity of poly(methyl methacrylate) on its miscibility with chlorinated polymers. *Macromolecules* **1988**, *21*, 2148–2154.
- (11) Zhao, Y.; Prud'homme, R. E. A nonradiative energy transfer fluorescence study: blends of poly(vinyl chloride) and poly(methyl methacrylates) of different tacticities and molecular weights. *Macromolecules* **1990**, *23*, 713–718.
- (12) Eijkelenboom, A. P. A. M.; Maas, W. E. J. R.; Veeman, W. S.; Buning, G. H. W.; Vankan, J. M. J. Triple-resonance fluorine-19, proton, and carbon-13 CP-MAS NMR study of the influence of PMMA tacticity on the miscibility in PMMA/poly(vinylidene fluoride) (PVF2) blends. *Macromolecules* **1992**, *25*, 4511–4518.
- (13) Kyu, T.; Ko, C.-C.; Lim, D.-S.; Smith, S. D.; Noda, I. Miscibility studies on blends of polycarbonate with syndiotactic polymethyl methacrylate. *J. Polym. Sci., Part B: Polym. Phys.* **1993**, *31*, 1641–1648.
- (14) Jong, L.; Pearce, E. M.; Kwei, T. N.m.r. study of hydrogen bonded polymer blends: influence of the tacticity of poly(methyl methacrylate) on its miscibility with poly(styrene-co-vinylphenol). *Polymer* **1993**, *34*, 48–55.

- (15) Honeycutt, J. D. A Theoretical Study of Tacticity Effects on Poly(vinyl chloride)/Poly(methyl methacrylate) Miscibility. *Macromolecules* **1994**, *27*, 5377–5381.
- (16) Hsu, W.-P. Effect of tacticity of poly(methyl methacrylate) on the miscibility with poly(styrene-co-acrylonitrile). *J. Appl. Polym. Sci.* **1999**, *74*, 2894–2899.
- (17) Hamon, L.; Grohens, Y.; Soldera, A.; Holl, Y. Miscibility in blends of stereoregular poly(methyl methacrylate)/poly(ethylene oxide) based oligomers. *Polymer* **2001**, *42*, 9697–9703.
- (18) Higgins, J. S.; Benoît, H. *Polymers and neutron scattering*; Clarendon Press: Oxford, 1994.
- (19) Yasuda, H.; Yamamoto, H.; Yamashita, M.; Yokota, K.; Nakamura, A.; Miyake, S.; Kai, Y.; Kanehisa, N. Synthesis of high molecular weight poly(methyl methacrylate) with extremely low polydispersity by the unique function of organolanthanide(III) complexes. *Macromolecules* **1993**, *26*, 7134–7143.
- (20) Biroš, J.; Larina, T.; Trekoval, J.; Pouchlý, J. Dependence of the glass transition temperature of poly(methyl methacrylates) on their tacticity. *Colloid Polym. Sci.* **1982**, *260*, 27–30.
- (21) Ute, K.; Miyatake, N.; Hatada, K. Glass transition temperature and melting temperature of uniform isotactic and syndiotactic poly(methyl methacrylate)s from 13mer to 50mer. *Polymer* **1995**, *36*, 1415–1419.
- (22) Robeson, L. M. *Polymer Blends*; Carl Hanser Verlag GmbH Co. KG, 2007.
- (23) Ma, W.; Yang, C.; Heeger, A. Spatial Fourier-Transform Analysis of the Morphology of Bulk Heterojunction Materials Used in “Plastic” Solar Cells. *Adv. Mater.* **2007**, *19*, 1387–1390.
- (24) Cabral, J. T.; Higgins, J. S. Small Angle Neutron Scattering from the Highly Interacting Polymer Mixture TMPC/PSd: No Evidence of Spatially Dependent Parameter. *Macromolecules* **2009**, *42*, 9528–9536.
- (25) Cabral, J. T.; Higgins, J. S. Spinodal nanostructures in polymer blends: On the validity of the Cahn-Hilliard length scale prediction. *Prog. Polym. Sci.* **2018**, *81*, 1–21.
- (26) Higgins, J. S.; Fruitwala, H.; Tomlins, P. E. Correlation of phase-separation behavior in polymer blends with thermodynamic measurements in the one-phase region. *Macromolecules* **1989**, *22*, 3674–3681.
- (27) Altstädt, V.; de Freitas, L. L.; Schubert, D. W. Rheological and mechanical properties of poly( $\alpha$ -Methylstyrene-co-Acrylonitrile)/poly(methylacrylate-co-methyl methacrylate) blends in miscible and phase-separated regimes of various morphologies. *Pure Appl. Chem.* **2004**, *76*, 389–413.
- (28) Aoki, Y.; Wang, H.; Sharratt, W.; Dalgliesh, R. M.; Higgins, J. S.; Cabral, J. T. Small Angle Neutron Scattering Study of the Thermodynamics of Highly Interacting PM-SAN/dPMMA Blends. *Macromolecules* **2019**, *52*, 1112–1124.
- (29) Wang, M.; Braun, H.-G.; Meyer, E. Crystalline structures in ultrathin poly(ethylene oxide)/poly(methyl methacrylate) blend films. *Polymer* **2003**, *44*, 5015–5021.
- (30) Tanaka, K.; Takahara, A.; Kajiyama, T. Film Thickness Dependence of the Surface Structure of Immiscible Polystyrene/Poly(methyl methacrylate) Blends. *Macromolecules* **1996**, *29*, 3232–3239.
- (31) Cabral, J. T. *Polymer Blends: Equilibrium, Dynamics and Phase Separation*. Ph.D. thesis, Imperial College: London, 2002.
- (32) Arnold, O.; et al. Mantid-Data analysis and visualization package for neutron scattering and SR experiments. *Nucl. Instrum. Methods Phys. Res., Sect. A* **2014**, *764*, 156–166.
- (33) Fox, T. G. Influence of Diluent and of Copolymer Composition on the Glass Temperature of a Polymer System. *Bull. Am. Phys. Soc.* **1956**, *1*, 123.
- (34) De Gennes, P.-G. *Scaling concepts in polymer physics*; Cornell University Press, 1979.
- (35) Sakurai, S.; Hasegawa, H.; Hashimoto, T.; Hargis, I. G.; Aggarwal, S. L.; Han, C. C. Microstructure and isotopic labeling effects on the miscibility of polybutadiene blends studied by the small-angle neutron scattering technique. *Macromolecules* **1990**, *23*, 451–459.
- (36) Freed, K. F. *Renormalization Group Theory of Macromolecules*; John Wiley Sons Inc: New York, 1987; p 361.
- (37) Doi, M. *Introduction to Polymer Physics*; Oxford University Press: Oxford, 1996; p 136.
- (38) Eitouni HB, B. N. *Physical Properties of Polymers Handbook*; AIP Press, New York: 2007.
- (39) Cahn, J. W.; Hilliard, J. E. Free Energy of a Nonuniform System. I. Interfacial Free Energy. *J. Chem. Phys.* **1958**, *28*, 258–267.
- (40) Cahn, J. W.; Hilliard, J. E. Free Energy of a Nonuniform System. III. Nucleation in a Two-Component Incompressible Fluid. *J. Chem. Phys.* **1959**, *31*, 688–699.
- (41) Cook, H. Brownian motion in spinodal decomposition. *Acta Metallurgica* **1970**, *18*, 297–306.
- (42) Binder, K.; Frisch, H. L.; Jäckle, J. Kinetics of phase separation in the presence of slowly relaxing structural variables. *J. Chem. Phys.* **1986**, *85*, 1505–1512.
- (43) Rapp, T. J.; Balsara, N. P. Does coarsening begin during the initial stages of spinodal decomposition. *J. Chem. Phys.* **2005**, *122*, No. 214903.
- (44) Bates, F. S.; Wiltzius, P. Spinodal decomposition of a symmetric critical mixture of deuterated and protonated polymer. *J. Chem. Phys.* **1989**, *91*, 3258–3274.
- (45) Jinnai, H.; Hasegawa, H.; Hashimoto, T.; Han, C. C. Time-resolved small-angle neutron scattering study of spinodal decomposition in deuterated and protonated polybutadiene blends. I. Effect of initial thermal fluctuations. *J. Chem. Phys.* **1993**, *99*, 4845–4854.
- (46) Strobl, G. R. Structure evolution during spinodal decomposition of polymer blends. *Macromolecules* **1985**, *18*, 558–563.
- (47) Han, C. C.; Akcasu, A. Z. Phase Decomposition in Polymers. *Annu. Rev. Phys. Chem.* **1992**, *43*, 61–90.
- (48) Schwahn, D.; Janssen, S.; Springer, T. Early state of spinodal decomposition studied with small angle neutron scattering in the blend deuteropolystyrene and polyvinylmethylether: A comparison with the Cahn-Hilliard-Cook theory. *J. Chem. Phys.* **1992**, *97*, 8775–8788.
- (49) Wang, Z.-G. Concentration fluctuation in binary polymer blends: parameter, spinodal and Ginzburg criterion. *J. Chem. Phys.* **2002**, *117*, 481–500.
- (50) Bates, F. S.; Fredrickson, G. H. Block Copolymer Thermodynamics: Theory and Experiment. *Annu. Rev. Phys. Chem.* **1990**, *41*, 525–557.
- (51) Hair, D. W.; Hobbie, E. K.; Nakatani, A. I.; Han, C. C. Deviation from mean-field behavior in a low molecular weight critical polymer blend. *J. Chem. Phys.* **1992**, *96*, 9133–9137.
- (52) Kim, E.; Kramer, E. J.; Wu, W. C.; Garrett, P. D. Diffusion in blends of poly(methyl methacrylate) and poly(styrene-co-acrylonitrile). *Polymer* **1994**, *35*, 5706–5715.
- (53) Zhang, H.; Lamnawar, K.; Maazouz, A. Rheological Modeling of the Mutual Diffusion and the Interphase Development for an Asymmetrical Bilayer Based on PMMA and PVDF Model Compatible Polymers. *Macromolecules* **2013**, *46*, 276–299.
- (54) Carmesin, H. O.; Heermann, D. W.; Binder, K. Influence of a continuous quenching procedure on the initial stages of spinodal decomposition. *Z. Phys. B: Condens. Matter* **1986**, *65*, 89–102.